Deep-learning-based inverse design of phononic crystals for anticipated wave attenuation

View Online   Export Citation   CrossMark

Sihao Han, Qiang Han, and Chunlei Li[a]

AFFILIATIONS

Department of Engineering Mechanics, School of Civil Engineering and Transportation, South China University of Technology, Guangzhou 510640, China

[a] Author to whom correspondence should be addressed: lichunlei@scut.edu.cn

ABSTRACT

Bandgaps of phononic crystals dominating the propagation of evanescent waves have received significant attention recently, which can be determined and tuned by the topology of a unit cell. Predicting a band structure and designing topological structures with desirable characteristics have become a research hotspot. In this study, a data-driven deep learning framework is applied to arrive at the prediction of the band structure and the inverse design of topology. A convolutional neural network is trained to predict band structures of phononic crystals. After training a generative adversarial network, the generator is concatenated with the convolutional neural network for inverse design. Meanwhile, a complex band structure of phononic crystals is computed by the periodic spectral finite element method to present the spatial decay of evanescent waves. The topology with the greater spatial attenuation is screened from the ground truth topology and the inversely designed topology. Finally, an optimized topological phononic crystal with an anticipated bandgap is obtained, which has the potential for better acoustic insulation and vibration isolation.

Published under an exclusive license by AIP Publishing. https://doi.org/10.1063/5.0111182

I. INTRODUCTION

Phononic Crystals (PnCs)[1] are usually periodic artificial composites made up of one or more materials with different physical properties and have extraordinary characteristics mainly depending on the lattice geometry. By designing the lattice structures of PnCs, the wave characteristics can be controlled to exhibit bandgap,[2,3] negative refraction,[4,5] bidirectional asymmetric propagation behavior,[6,7] and Dirac-like cones,[8,9] among many others.

Over the past few decades, research focusing on bandgaps has proliferated due to Bragg scattering and local resonance.[10–12] The interaction of acoustic/elastic waves with heterogeneous periodic structures results in constructive reflection and superposition of reflected waves, thus preventing the propagation of acoustic/elastic waves in the bandgap frequency range. However, previous studies have shown that the propagation of acoustic/elastic waves is not completely stopped in the bandgap frequency range[13–15] but is attenuated to some extent. These waves are called evanescent waves. Romero-García et al.[16–18] pointed out that the evanescent waves decay exponentially within the bandgap and the attenuation degrees are determined by the minimum imaginary parts of the wave numbers. The classic method of calculating the band properties of

PnCs is to solve the frequencies of propagating waves when Bloch wave numbers k are given. It is called the $\omega(k)$ method. However, because the method only calculates the real band properties of PnCs, it fails to reveal the decay of evanescent waves. Therefore, in order to adequately describe the propagating characteristics of evanescent waves, it is necessary to compute the complex band structure by solving the wave numbers at the given frequencies. This approach is known as the $k(\omega)$ method. Laude et al.[19] used the extended plane-wave expansion (EPWE) to obtain complex band structures of PnCs. Veres and Berer[20] used a semi-analytical finite element (SAFE) method to investigate complex band structures of surface PnCs with one-dimensional periodicity in the frequency domain. In the periodic direction, the investigation is simplified to the irreducible first Brillouin zone by using periodic boundary conditions. In the periodic direction, wave propagation is unrestricted so that PnCs can be modeled by the SAFE method using a harmonic *Ansatz*. Based on the Bloch theorem and the higher-order spectral elements, Li et al.[21] proposed a semi-analytical periodic spectral finite element (Per-SFE) method to investigate dispersion and bandgaps of elastic guided waves in the periodic composite plates. In this work, this method is also utilized to calculate the complex band structure and dispersion

relations of two-dimensional PnCs with one-dimensional periodicity. By calculating the complex band structure, the imaginary parts are analyzed in order to reveal the spatial decay of evanescent waves in the PnCs.

The material distribution of a unit cell played an important role in the bandgap characteristics of PnCs. Therefore, the most considerable current discussion in tunable bandgap is optimization and design of the lattice unit cell. In the past years, topology optimization has been successfully applied in structural optimization and inverse design of PnCs.[22–25] However, there remains a difficulty in accurately manipulating the band structures and wave propagation by using the current topology optimization methods. Recently, unprecedented advances in deep learning (DL) have made it possible to achieve precise and efficient band structure prediction and inverse design of PnCs.[26–29] Li *et al.*[30] trained an auto-encoder (AE) to extract the topological features from the lattice of PnCs and trained a multi-layer perceptron (MLP) to establish the intrinsic relationship between band structures and topological features. The trained model was eventually employed to design PnCs with anticipated bandgaps. Jiang *et al.*[31] proposed the conceptual framework for DL, that is, they utilized the convolutional neural network (CNN) and the condition generative adversarial network (cGAN) to establish mapping relationships between the structural topology and the band structure of PnCs. This work efficiently realized the forward prediction of dispersion relations, inverse generation of structural configurations, and proactive inverse design for re-customized targets of PnCs composed of composite materials.

For achieving the optimal topology of PnCs with anticipated attenuation characteristics, the complex band structure of one-dimensional periodic two-dimensional tetragonal symmetric solid–solid PnCs is considered and three primary issues are addressed as follows: (a) predicting the real band structures of PnCs, (b) inversely designing the topological structures of PnCs by real band structures, and (c) screening a topological structure of the PnCs with greater wave attenuation in the imaginary part of the first bandgap. In addition, the content can be organized in the following scheme. Section II concerns with the Per-SFE approach employed for calculating the complex band structures of PnCs. The fundamental concepts and architectural details of the adopted DL models utilized in this study are described in Sec. III. Section IV elaborated on the process of data preparation, model training, result validation, and topology screening. Section V summarized the conclusion of this study.

II. ELASTIC WAVE MODELING FOR THE ONE-DIMENSIONAL PHONONIC CRYSTALS

A. The periodic spectral finite element (Per-SFE) approach

In this study, the Per-SFE method is applied to compute the complex band structure of two-dimensional tetragonal symmetric solid–solid PnCs by the $k(\omega)$ technique. The PnCs exhibit the repetitive periodic feature in the x direction and the topology of a unit cell of the PnCs is a two-dimensional structure on an $x - y$ plane (as shown in Fig. 1). It is assumed that elastic waves propagate in the x direction [as depicted in Fig. 1(b)]. The harmonic ansatz is employed to describe the waveform in the propagation direction, the nodal displacement field in an element is expressed as

$$\mathbf{u}^e(\mathbf{x}, \mathbf{y}, \mathbf{t}) = \mathbf{N}(\mathbf{x}, \mathbf{y})\,\mathbf{Q}^e e^{i(kx-\omega t)}, \tag{1}$$

where $\mathbf{N}(\mathbf{x}, \mathbf{y})$ denotes the matrix of the shape functions (the detailed description of higher-order shape functions can be found in the literature) and $\mathbf{Q}^e$ denotes the nodal displacements of any point in an element. In the calculation, the plane strain assumption is adopted, so the stiffness matrix is

$$\mathbf{C}_i = \frac{E_i}{(1+\mu_i)(1-2\mu_i)}\begin{bmatrix} 1-\mu_i & \mu_i & 0 \\ \mu_i & 1-\mu_i & 0 \\ 0 & 0 & \frac{1-2\mu_i}{2} \end{bmatrix}, \quad (i=1,2), \tag{2}$$

where $\mathbf{C}_i$, E_i, and μ_i ($i = 1, 2$) denote the material properties of the two materials in PnCs, respectively, as listed in Table I for details. Displacement $\mathbf{u}^e$, strain $\boldsymbol{\varepsilon}^e$, and stress vectors $\boldsymbol{\sigma}^e$ in an element are given by

$$\mathbf{u}^e(\mathbf{x}, \mathbf{y}) = \begin{bmatrix} u^e(x, y) & v^e(x, y) \end{bmatrix}^T, \tag{3}$$

$$\boldsymbol{\varepsilon}^e = \begin{bmatrix} \varepsilon_{xx} & \varepsilon_{yy} & \gamma_{xy} \end{bmatrix}^T, \tag{4}$$

$$\boldsymbol{\sigma}^e = \begin{bmatrix} \sigma_{xx} & \sigma_{yy} & \tau_{xy} \end{bmatrix}^T. \tag{5}$$

The discretized material law and the kinematic relations are given for one element as follows:

$$\boldsymbol{\varepsilon}^e = \mathbf{L}\,\mathbf{u}^e = \mathbf{L}\mathbf{N}\,\mathbf{Q}^e e^{i(kx-\omega t)}, \tag{6}$$

$$\boldsymbol{\sigma}^e = \mathbf{C}\boldsymbol{\varepsilon}^e = \mathbf{C}\mathbf{L}\mathbf{N}\,\mathbf{Q}^e e^{i(kx-\omega t)}, \tag{7}$$

with the amplitude vector of nodal displacement $\mathbf{Q}^e$,

$$\mathbf{Q^e} = \begin{bmatrix} u_1 & v_1 & u_2 & v_2 & u_3 & v_3 & u_4 & v_4 \end{bmatrix}^T. \tag{8}$$

The elastic strain operator matrix $\mathbf{L}$ and the matrix of the shape functions $\mathbf{N}$ are expressed as

$$\mathbf{L} = \frac{\partial}{\partial x}\,\mathbf{L_x} + \frac{\partial}{\partial y}\,\mathbf{L_y}, \tag{9}$$

$$\mathbf{N} = \begin{bmatrix} N_1 & 0 & N_2 & 0 & N_3 & 0 & N_4 & 0 \\ 0 & N_1 & 0 & N_2 & 0 & N_3 & 0 & N_4 \end{bmatrix}, \tag{10}$$

with

$$\mathbf{L_x} = \begin{bmatrix} 1 & 0 & 0 \\ 0 & 0 & 1 \end{bmatrix}^T, \tag{11}$$

$$\mathbf{L_y} = \begin{bmatrix} 0 & 0 & 1 \\ 0 & 1 & 0 \end{bmatrix}^T. \tag{12}$$
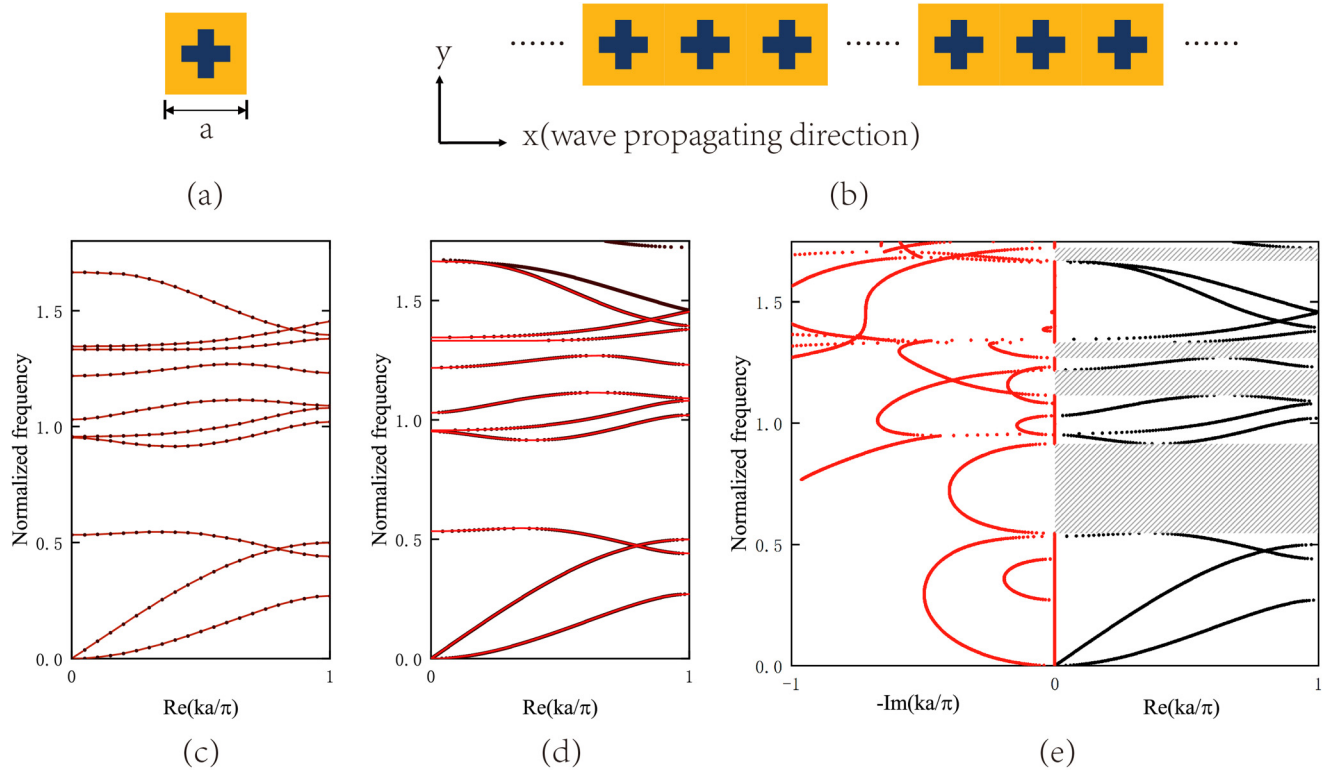
FIG. 1. Geometric model of PnCs and complex band structure by the Per-SFE method. (a) The two-dimensional unit cell of a PnC. The yellow area denotes epoxy and the dark blue area denotes steel. The lattice constant is *a*. (b) The Per-SFE wave simulation model of the PnCs. The model is infinitely periodic in the *x* direction. (c) The classic band structure of the PnC calculated by the $\omega(k)$ method. (d) The real part of the complex band structure of the PnC calculated by the $k(\omega)$ method, denoted by black curves. Red curves represent the classic band structure of the PnC. (e) The complex band structure of the PnC. The bandgaps are marked by gray slash areas.

Substituting Eqs. (9) and (10) into Eq. (6) leads to the following relation:

$$\varepsilon^e = \mathbf{L}\mathbf{u}^e = (\mathbf{B}_1 + ik\mathbf{B}_2)\mathbf{Q}^e e^{i(kx-\omega t)}, \tag{13}$$

with the strain–displacement matrices

$$\mathbf{B}_1 = \mathbf{L_x}\frac{\partial \mathbf{N}(\mathbf{x,y})}{\partial x} + \mathbf{L_y}\frac{\partial \mathbf{N}(\mathbf{x,y})}{\partial y}, \tag{14}$$

$$\mathbf{B}_2 = \mathbf{L_x}\mathbf{N}. \tag{15}$$

TABLE I. Material properties of the phononic crystal.

Materials	Young's modulus (E) (Pa)	Poisson's ratio (μ)	Density (ρ) (kg/m³)
Steel	2.10×10^{11}	0.3	7780
Epoxy	4.35×10^{9}	0.368	1180

Through the virtual work principle, the governing equation of wave motion in the PnCs can be expressed as

$$\int_\Gamma \delta(\mathbf{u}^e)^T \mathbf{t}^e d\Gamma = \int_V \delta(\mathbf{u}^e)^T(\rho^e \ddot{u}^e)dV + \int_V \delta(\mathbf{u}^e)^T C\varepsilon^e dV, \tag{16}$$

where $\delta\mathbf{u}$ and $\delta\boldsymbol{\varepsilon}$ represent virtual displacement and virtual strain, respectively. $\ddot{u}$ is a second derivative of displacement with respect to time in an element, Γ is the surface of the element, and V is the volume of the element. $\mathbf{t}^e$ represents the external traction vector that can also be expressed using shape functions and nodal external tractions $\mathbf{T}^e$, that is,

$$\mathbf{t}^e = \mathbf{N}(x,y)\mathbf{T}^e e^{i(kx-\omega t)}. \tag{17}$$

Substituting Eqs. (1), (13), and (17) into Eq. (16) yields

$$\int_\Gamma \delta(\mathbf{Q}^e)^T \mathbf{N}^T \mathbf{N}\mathbf{T}^e d\Gamma = \int_V \delta(\mathbf{Q}^e)^T \mathbf{N}^T(-k^2\rho^e \mathbf{N}\mathbf{Q}^e)dV$$
$$+ \int_V \delta(\mathbf{Q}^e)^T[(\mathbf{B}_1 - ik\mathbf{B}_2)]^T \mathbf{C}^e(\mathbf{B}_1 + ik\mathbf{B}_2)\mathbf{Q}^e dV. \tag{18}$$

Equation (18) is satisfied for any arbitrarily chosen virtual displacement. Thus, the virtual displacement term $\delta(\mathbf{Q}^e)^T$ can be eliminated from Eq. (18),

$$\int_\Gamma \mathbf{N}^T \mathbf{N} \mathbf{T}^e d\Gamma = \int_V \mathbf{N}^T \left(-k^2 \rho^e \, \mathbf{N} \, \mathbf{Q}^e\right) dV$$
$$+ \int_V \left[(\mathbf{B}_1 - ik \, \mathbf{B}_2)\right]^T \mathbf{C}^e (\mathbf{B}_1 + ik \, \mathbf{B}_2) \, \mathbf{Q}^e dV. \quad (19)$$

The linear elements used here [Eq. (19)] can, thus, be further simplified to

$$\mathbf{F}^e = \left(\mathbf{K}_0^e + ik \, \mathbf{K}_1^e + k^2 \, \mathbf{K}_3^e\right) \mathbf{Q}^e - \omega^2 \, \mathbf{M}^e \, \mathbf{Q}^e \quad (20)$$

and the force vector and the element matrices

$$\mathbf{F}^e = \int_{V_0} \mathbf{N}^T \mathbf{N} \mathbf{T}^e dV, \quad (21)$$

$$\mathbf{K}_0^e = \int_{V_0} \left(\mathbf{B}_1{}^T \mathbf{C}^e \mathbf{B}_1\right) dV, \quad (22)$$

$$\mathbf{K}_1^e = \int_{V_0} \left(\mathbf{B}_2{}^T \mathbf{C}^e \mathbf{B}_1 - \mathbf{B}_1{}^T \mathbf{C}^e \mathbf{B}_2\right) dV, \quad (23)$$

$$\mathbf{K}_2^e = \int_{V_0} \left(\mathbf{B}_2{}^T \mathbf{C}^e \mathbf{B}_2\right) dV, \quad (24)$$

$$\mathbf{M}^e = \int_{V_0} \mathbf{N}^T \rho \, \mathbf{N} dV. \quad (25)$$

Equations (21)–(25) can be evaluated numerically for each element. Assembling all the elements and applying the traction-free boundary conditions on the top and bottom surfaces of the PnCs, one can form an eigenvalue problem in the global coordinate system,

$$\left(\mathbf{K}_0 + ik \, \mathbf{K}_1 + k^2 \, \mathbf{K}_2 - \omega^2 \, \mathbf{M}\right) \mathbf{Q} = 0. \quad (26)$$

In the periodic direction, the addition of Bloch–Floquet boundary conditions converted the reduced displacement of nodes on the right boundary to the left boundary. In stiffness matrix $\mathbf{K}_i$ ($i = 0, 1, 2$), mass matrix $\mathbf{M}$, and after rearrangement by a transformation matrix, the displacement amplitude vector $\mathbf{Q}$ can be expressed as follows:

$$\tilde{K}_i = \mathbf{H}^T \mathbf{K}_i \mathbf{H}, \quad (i = 0, 1, 2), \quad (27)$$

$$\tilde{M} = \mathbf{H}^T \mathbf{M} \mathbf{H}, \quad (28)$$

$$\tilde{Q} = \mathbf{H}^T \mathbf{Q} \mathbf{H}. \quad (29)$$

Substituting Eqs. (27)–(29) into Eq. (26) leads to a second-order polynomial eigenvalue problem with regard to wave dispersion,

$$\left(\tilde{K}_0 + ik \, \tilde{K}_1 + k^2 \, \tilde{K}_2 - \omega^2 \, \tilde{M}\right) \tilde{Q} = 0. \quad (30)$$

By matrix transformation, the generalized eigenvalue problem can be simplified into the standard eigenvalue problem

$$-\mathbf{A}\psi = \lambda\psi, \quad (31)$$

with

$$\mathbf{A} = \begin{bmatrix} \tilde{K}_3^{-1} \tilde{K}_2^T & -\tilde{K}_3^{-1} \\ \omega^2 \tilde{M} - \tilde{K}_1 + \tilde{K}_2 \tilde{K}_3^{-1} \tilde{K}_3^T & -\tilde{K}_2 \tilde{K}_3^{-1} \end{bmatrix}, \quad (32)$$

$$\psi = \begin{bmatrix} \tilde{u} & \tilde{q} \end{bmatrix}^T, \quad (33)$$

$$\lambda = ik, \quad (34)$$

where $\mathbf{q}$ is the force vector. For traversing the given angular frequency ω, the eigenvalue wavenumbers k can be computed explicitly. For wave propagation in the PnCs, the variation curves of wavenumbers with angular frequency demonstrate dispersion characteristics of elastic guided waves. This periodic spectral finite element method is often referred to as $k(\omega)$ method, as the wave number is evaluated as a function of the angular frequencies. In this work, this approach is utilized to obtain a complex band structure of the phononic crystals with different topologies, and imaginary wavenumbers in a band structure represent the degree of wave attenuation in phononic crystals.

B. Calculation of the complex band structure

In this study, the material properties of the two-dimensional tetragonal symmetric solid–solid PnCs are shown in Table I and the lattice length $a = 1$ mm. Figure 1(c) shows the classic band structure of the PnC in Fig. 1(a) calculated by the $\omega(k)$ method by means of the Per-SFE method. The wave vector $\mathbf{k}$ is normalized to $\bar{k} = \mathbf{k}a/\pi \in [0, 1]$ by the lattice length a. At the same time, the frequencies are normalized to $\Omega = fa/c_t$ by period a and shear wave velocity in epoxy c_t. During the calculation, the frequencies were scanned every 0.05 times, and the band structure of the first ten modes was calculated in total. So, a total of 21×10 eigenfrequencies points were obtained. All points are marked with black dots in Fig. 1(c), and the red curves are the dispersion curves of the connection. The black curves in Fig. 1(d) are the real part of the complex band structure of the PnC in Fig. 1(a) computed by the $k(\omega)$ method applying the Per-SFE method. Compared with the classic band structure calculated by the $\omega(k)$ method (marked by the red curves in the figure), both are exactly identical. Figure 1(e) shows the real and imaginary parts of the complex band structure. As can be seen, the minimum value of the imaginary part is always zero when there is no bandgap in the real part. The minimum value of the imaginary part of the complex band structure is no longer zero when a bandgap exists. These complex bands are termed with evanescent Bloch waves with nonzero imaginary parts of the wave vectors and their spatial decay are determined by the value of their imaginary parts. The more evanescent waves are attenuated, the greater the minimum value of the imaginary part is. The complex band structure evidently confirms the

occurrence of bandgaps owing to the evanescent character of Bloch waves rather than the absence of bands.

III. DEEP LEARNING MODELS

This section describes the DL model adopted in this study and its training details. Two algorithms, regression and generation, are used to predict the band structure and to inversely design the topological structure of the unit cell of the PnCs by DL. Both algorithms are implemented by CNN and GAN, respectively. The CNN is utilized to predict the band structure from the topological structure of the unit cell, and the GAN is utilized to generate the topological structure from the band structure. After training the two DL models separately, the two parts are serialized together to implement the inverse design. The computer CPU is Intel(R) Core(TM) I7-11700K @ 3.60 GHz, and the GPU is NVIDIA GeForce RTX 2060 (12 GB) was utilized in computing training datasets and training DL models. The software that does the CNN and GAN code execution is

Microsoft VS Code and the DL framework is PyTorch. In the process of completing the work, we used many open source extension packages of python, the main ones are Numpy and Scipy.

A. Architecture and training details of the CNN

The initial step in this study is to apply CNN to predict the band structure of the PnCs [Fig. 2(a)]. The nonlinear mapping relationship between the matrix representing topological structures of a unit cell of the PnCs and the matrix representing its band structure can be established by the CNN. The advantage of using CNN rather than classic simulation methods is that it bypasses the complicated physical mechanism to make predictions directly based on the data features extracted from massive data. As mentioned in Sec. II, this study focused on the first ten modes of elastic waves in PnCs. By observing the calculation results of the datasets, it is found that the PnCs model in this study has a smaller frequency distribution for the first few modes and a wider frequency
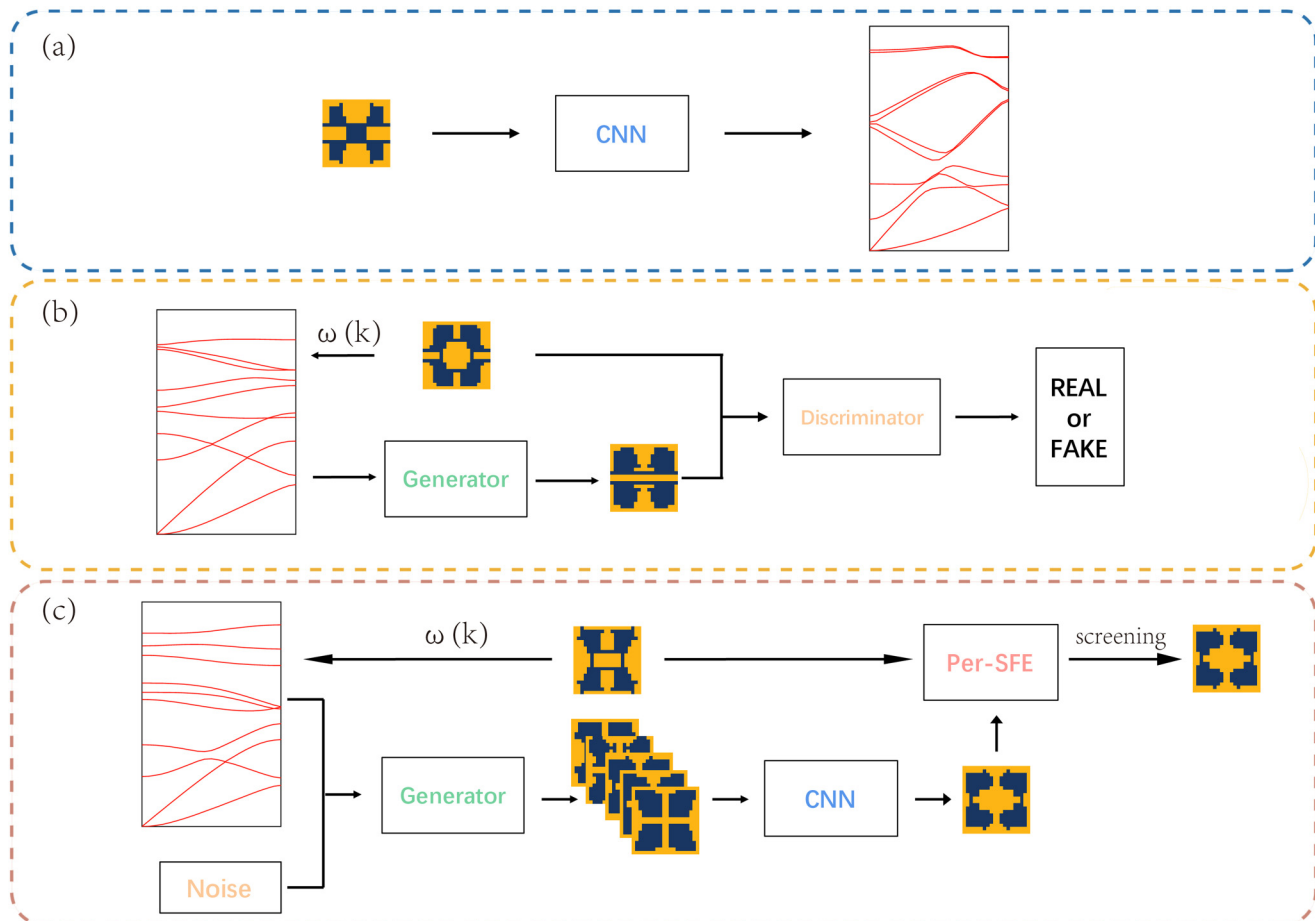

FIG. 2. Workflow of the design of PnCs based on the DL. (a) Schematic of the CNN applied for the band structure prediction. (b) Schematic of the GAN applied for topology generation. (c) Schematic of the DL framework applied for inverse design.

TABLE II. Details of the CNN.

Type	Kernel or pool size	Stride	Padding	Output size
Convolution	5×5	1	2	$1 \times 128 \times 20 \times 20$
ReLU				$1 \times 128 \times 20 \times 20$
MaxPool	2×2	2	0	$1 \times 128 \times 10 \times 10$
Convolution	3×3	1	1	$1 \times 512 \times 10 \times 10$
ReLU				$1 \times 512 \times 10 \times 10$
MaxPool	2×2	2	0	$1 \times 512 \times 5 \times 5$
Convolution	3×3	1	1	$1 \times 512 \times 5 \times 5$
ReLU				$1 \times 512 \times 5 \times 5$
Convolution	3×3	1	1	$1 \times 1024 \times 5 \times 5$
ReLU				$1 \times 1024 \times 5 \times 5$
MaxPool	2×2	2	0	$1 \times 1024 \times 3 \times 3$
AdaptiveAvgPool				$1 \times 1024 \times 3 \times 3$
Flatten				$1 \times (1024 \times 3 \times 3)$
Linear				1×4096
ReLU				1×4096
Linear				1×2048
ReLU				1×2048
Linear				1×21

distribution for the higher modes. As a result, we trained CNN to predict each model separately to improve the accuracy of the predictions. That is, while each mode is predicted by the constructed CNN with the same architecture, each network is trained separately. Table II shows the details of the CNN.

B. Architecture and training details of the GAN

In the second step, the GAN[32] model is applied to inversely generate the topological structures of the unit cell of PnCs inversely from their band structure, as shown in Fig. 2(b). The main focus of inverse generation is to obtain the features between the topological structures of PnCs and their band structures and to utilize these features to proactive inverse generate. DL has the advantage of powerful feature extraction capabilities. The GAN consists of two parts: generator and discriminator. The generator generates new data based on a given condition, with the purpose of generating samples that are as realistic as possible. The discriminator determines whether the data obtained are generated by the generator or existed initially in order to distinguish the generated sample as much as possible from the ground truth samples. The ultimate purpose of the entire GAN is to make it impossible for the discriminator to determine whether the sample is original or generated by the generator, thus obtaining new samples with the same characteristics as the ground truth data. The design of the GAN is based on the idea of game theory, in which the two networks work against each other, constantly adjusting parameters to finally achieve the desired purpose. In this study, the Pix2Pix[33] model, one of GAN, is applied to the inverse generation. It consists of the generating network U-Net and a discriminative network PatchGAN. Tables III and IV show the details of the U-Net and the PatchGAN used in this paper, respectively.

TABLE III. Details of the generator.

Type	Kernel or pool size	Stride	Padding	Output size
Convolution	1×1	1		$1 \times 21 \times 1 \times 20$
LeakyReLU				$1 \times 21 \times 1 \times 20$
Convolution	1×1	1		$1 \times 1 \times 20 \times 20$
LeakyReLU				$1 \times 1 \times 20 \times 20$
Convolution	3×3	1	1	$1 \times 64 \times 20 \times 20$
LeakyReLU				$1 \times 64 \times 20 \times 20$
Convolution	6×6	1	1	$1 \times 128 \times 17 \times 17$
BN and LeakyReLU				$1 \times 128 \times 17 \times 17$
Convolution	4×4	1	1	$1 \times 256 \times 16 \times 16$
BN and LeakyReLU				$1 \times 256 \times 16 \times 16$
Convolution	4×4	1	1	$1 \times 512 \times 15 \times 15$
BN and LeakyReLU				$1 \times 512 \times 15 \times 15$
Convolution	4×4	1	1	$1 \times 512 \times 14 \times 14$
BN and LeakyReLU				$1 \times 512 \times 14 \times 14$
Convolution	3×3	1	1	$1 \times 512 \times 14 \times 14$
BN and ReLU				$1 \times 512 \times 14 \times 14$
ConvTranspose	4×4	1	1	$1 \times 512 \times 15 \times 15$
BN and ReLU				$1 \times 512 \times 15 \times 15$
ConvTranspose	4×4	1	1	$1 \times 256 \times 16 \times 16$
BN and ReLU				$1 \times 256 \times 16 \times 16$
ConvTranspose	4×4	1	1	$1 \times 128 \times 17 \times 17$
BN and ReLU				$1 \times 128 \times 17 \times 17$
ConvTranspose	6×6	1	1	$1 \times 64 \times 20 \times 20$
BN and ReLU				$1 \times 64 \times 20 \times 20$
ConvTranspose	3×3	1	1	$1 \times 1 \times 20 \times 20$
Tanh				$1 \times 1 \times 20 \times 20$

C. Training details of the DL framework for inverse design

In the final step, we concatenate the generator of GAN and CNN for inverse design. The workflow is shown in Fig. 2(c). It should be noted that in the process of inverse design, the two networks themselves are not directly connected. Instead, the CNN training in Fig. 2(a) is performed first, and then the GAN training in Fig. 2(b) is performed. Finally, the trained CNN and the generator of GAN are taken out and connected in the way of Fig. 2(c) for

TABLE IV. Details of the discriminator.

Type	Kernel or pool size	Stride	Padding	Output size
Convolution	4×4	2	1	$1 \times 64 \times 10 \times 10$
LeakyReLU				$1 \times 64 \times 10 \times 10$
Convolution	4×4	1	1	$1 \times 128 \times 7 \times 7$
BN and LeakyReLU				$1 \times 128 \times 7 \times 7$
Convolution	4×4	1	1	$1 \times 256 \times 6 \times 6$
BN and LeakyReLU				$1 \times 256 \times 6 \times 6$
Convolution	4×4	1	1	$1 \times 512 \times 5 \times 5$
BN and LeakyReLU				$1 \times 512 \times 5 \times 5$
Convolution	4×4	1	1	$1 \times 1 \times 4 \times 4$

inverse design. In addition, we added random noise perturbations to the input of the generator that can generate multiple topological structures with similar band structure characteristics in the inverse design. The generated structures are then fed into the CNN to predict their band structures. Compared with the original input label band structures, the one with the least error is selected as the candidate obtained by inverse design. Finally, the topological structure with the larger wave attenuation was selected as the optimal structure under the similar bandgap by $k(\omega)$ technique applying the Per-SFE method. Due to the wide distribution of higher-order modes of each topology, it is difficult to obtain topological structures with the same higher-order modes accurately by GAN. Therefore, we only focus on the first bandgap created by the lower-order modes of PnCs.

IV. RESULTS AND DISCUSSIONS

In this section, the procedures for training and testing the CNN and the GAN are elaborated. The errors of these DL models

are analyzed. Thereafter, for topological structures of the unit cell with similar first bandgaps, the topological structure with greater wave attenuation is selected by the $k(\omega)$ technique utilizing the Per-SFE method.

A. Data preparation

In this study, the two-dimensional tetragonal symmetric solid–solid PnCs are generated by the twice specular symmetry method. To begin with, the unit cell of PnCs is discretized into 20×20 units in the calculation, represented by 0/1 matrix with the same size, where 0 stands for epoxy and 1 represents steel, as shown in Fig. 3(a). The specific process of generating a geometric model of PnCs is as follows: (a) A 0/1 matrix of 10×10 (i.e., 1/4 cell) was randomly generated as the initial subjects. Specifically, the ratio of the number of 0 and 1 is approximately 9:1 depending on the porosity requirement. (b) Morphological closed operation of the matrix using 5×5 sized square in the steel function of MATLAB resulted in 1/4 cell. (c) The final topology is obtained by means of
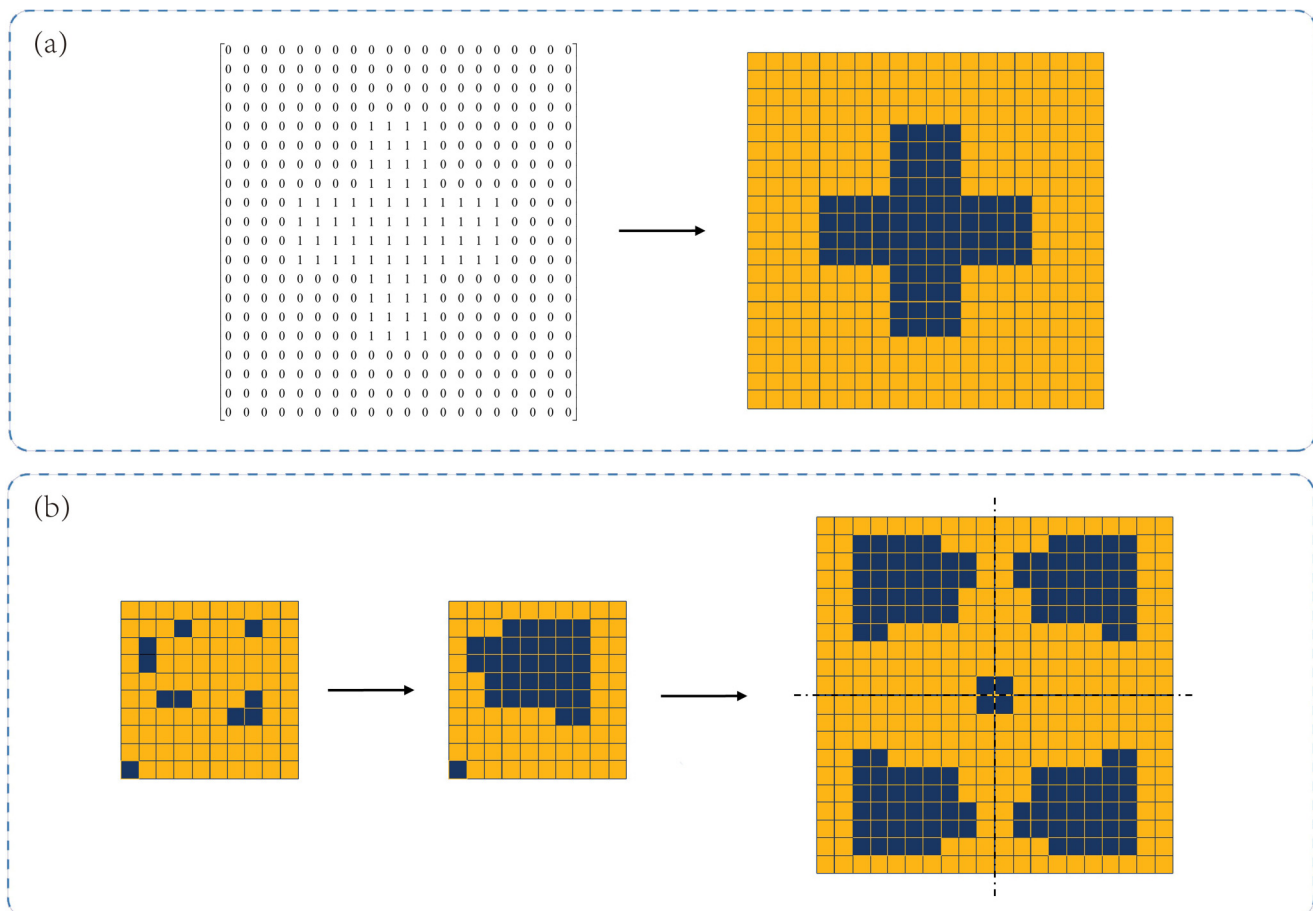

FIG. 3. Data preparation of unit cell mesh (a) The 0/1 matrix and its corresponding discretized unit cell of a PnC with the same size. (b) The schematic of the twice specular symmetry method for generating the unit cell of a PnC.

two mirror symmetries in the axial and longitudinal directions. Since the PnCs in this study were generated with different distributions of the two materials and do not have voids, connectivity is not a major issue in this problem. The topological structure generation process is shown in Fig. 3(b).

Due to the computational time and resource constraints, a total of 21 164 unique band structures with different topologies serve as datasets. The hold-out method[34] is adopted in the process of training DL model. The full dataset is randomly scrambled and divided into two mutually exclusive parts: 80% into training set and 20% into test set. In the parameter adjustment process, the training set is used to calculate the loss and update the parameters accordingly, without establishing the validation set. The test set is only used to test the results of the model and is not involved in the parameter adjustment process.

B. Forward prediction of band structures

In the forward prediction, the inputs of CNN are the topological structures of unit cell of PnCs, and the outputs are their corresponding band structures. The training epoch from scratch is 300, the batch size is 128, and the optimizer is the Stochastic Gradient Descent (SGD) with a weight decay of 1×10^{-5} and a momentum of 0.9. The learning rate starts at 0.1 and drops tenfold every 100 epochs. Figure 4(a) shows the result of the determination coefficient $R^2 = 0.9978$ between the eigenfrequencies predicted by CNN and those computed by the $\omega(k)$ method using the Per-SFE method, which is calculated by

$$R^2 = 1 - \frac{\Sigma(\omega_{ij} - \hat{\omega}_{ij})^2}{\Sigma(\omega_{ij} - \bar{\omega}_{ij})^2}, \quad (35)$$
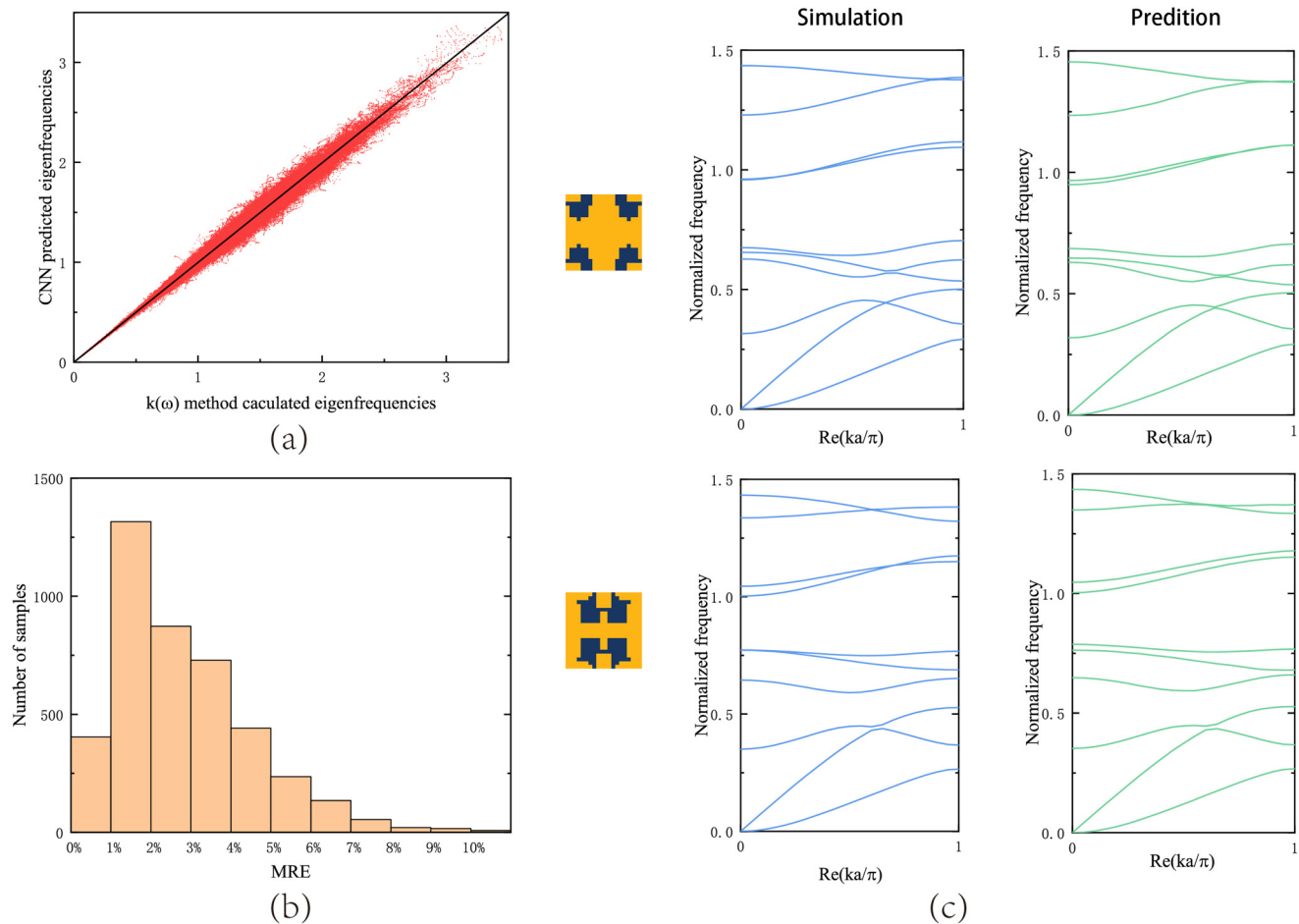

FIG. 4. CNN performance for predicting the band structure. (a) Comparisons between the eigenfrequencies predicted by CNN and simulated by the $\omega(k)$ method using the Per-SFE method. The determination coefficient $R^2 = 0.9978$. (b) MRE distribution of the test samples. (c) Random examples of the predicted band structure and the corresponding simulated band structure.

where w_{ij} and $\hat{w}_{ij}$ are the jth predicted eigenfrequency and jth simulated eigenfrequency of the ith test sample, respectively. $\bar{w}_{ij}$ is the average value of the simulated eigenfrequencies. In addition, it can be found that the prediction accuracy of high-order modes is lower than that of low-order modes because of their wider frequency distribution range. This confirms what we observed in Sec. III. The mean relative error (MRE) is employed to evaluate the error between the predicted band structure and the Per-SFE simulated band structure, which is defined as

$$MRE = \frac{1}{mn} \sum_{i=1}^{m} \sum_{j=1}^{n} \left| \frac{w_{ij} - \hat{w}_{ij}}{w_{ij}} \right| \times 100\%, \qquad (36)$$

where m and n are the number of test samples and the number of eigenfrequencies of the band structure, respectively. The distribution of the MRE is shown in Fig. 4(b). Figure 4(c) presents some random examples comparing the predicted band structure with the computed band structure. As can be observed, the predicted band structure is in good agreement with the calculated within a reasonable accuracy.

C. Inverse generation of topological structures

Having demonstrated the prediction of the band structures of PnCs with CNN, the Pix2Pix is utilized to achieve the inverse generation of the topological structures of unit cell. The Pix2Pix is trained for 2000 epochs using an Adam optimizer with a learning rate of 2×10^{-4} and a batch size of 512. Other parameters are consistent with those in the Pix2Pix manuscript.[33] The Pix2Pix is a partial adaptation of the classic cGAN. The input of cGAN is noise and the

output is image, while the input of Pix2Pix is the label image and the output is the generated image. At the same time, the loss function has also been modified. The generator loss G_{loss} is defined as

$$G_{loss} = E_{x,y}[\log(1 - D(y, G(x)))] + \lambda \| y - G(x) \|_1. \qquad (37)$$

The discriminator loss G_{loss} is defined as

$$D_{loss} = E_{x,y}[\log(D(y, G(x)))] + E_{y,y}[\log(1 - D(y, y))], \qquad (38)$$

where x is the input band structure, y is the topological structure, and λ is equal to 100.

Figure 5 shows the results of random selections, and there are two situations that can be observed. Figure 5(a) shows that an almost identical topology is generated by Pix2Pix from the band structure, while a different generated topology is shown in Fig. 5(b). In both situations, the band characteristics of original topologies and those of generated topologies are similar, especially for the lower modes. It is proved that there is a one-to-many relationship between the band structure and topological structure, which provided a possibility for inverse design and optimization. The details will be explained in Sec. IV D.

D. Inverse design of PnCs

Through the DL framework shown in Fig. 2(c), two candidate topologies with similar first bandgap can be obtained. Non-uniqueness is the nature of inverse design problems. Figure 6(a) shows a specific example. Based on the example in
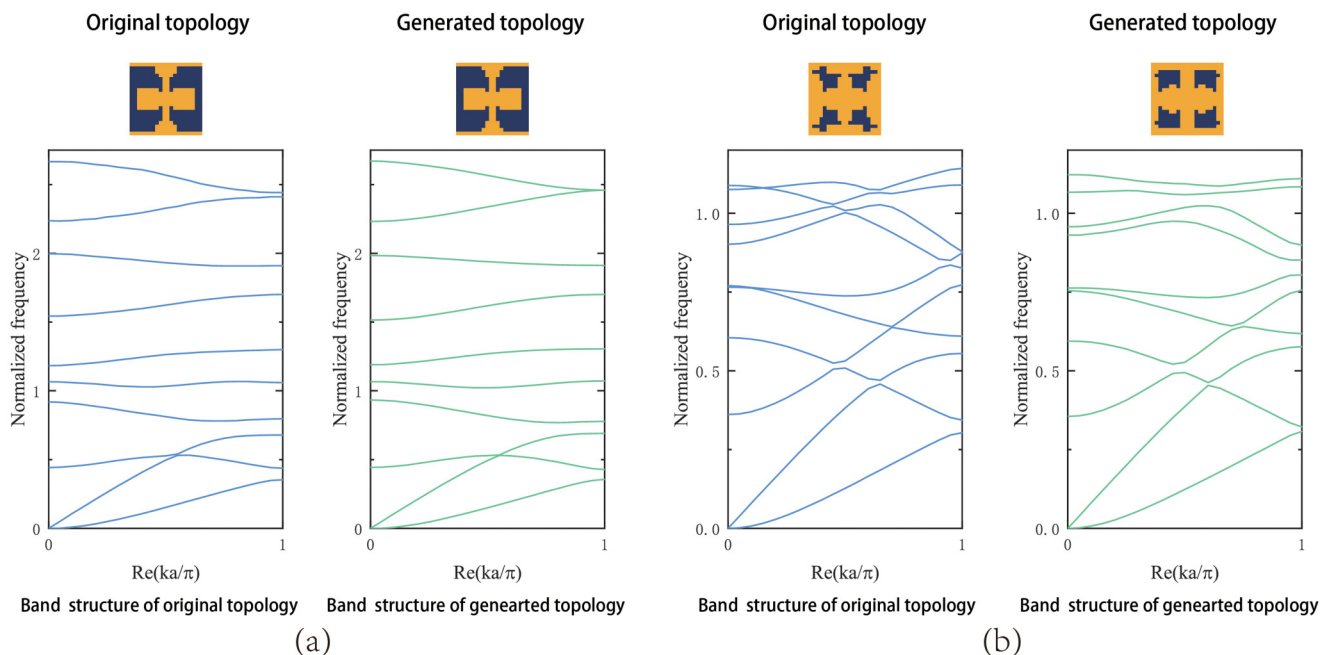

FIG. 5. Examples of the generated topologies and their band structures. (a) An example of generating a similar topology. (b) An example of generating diverse topology.
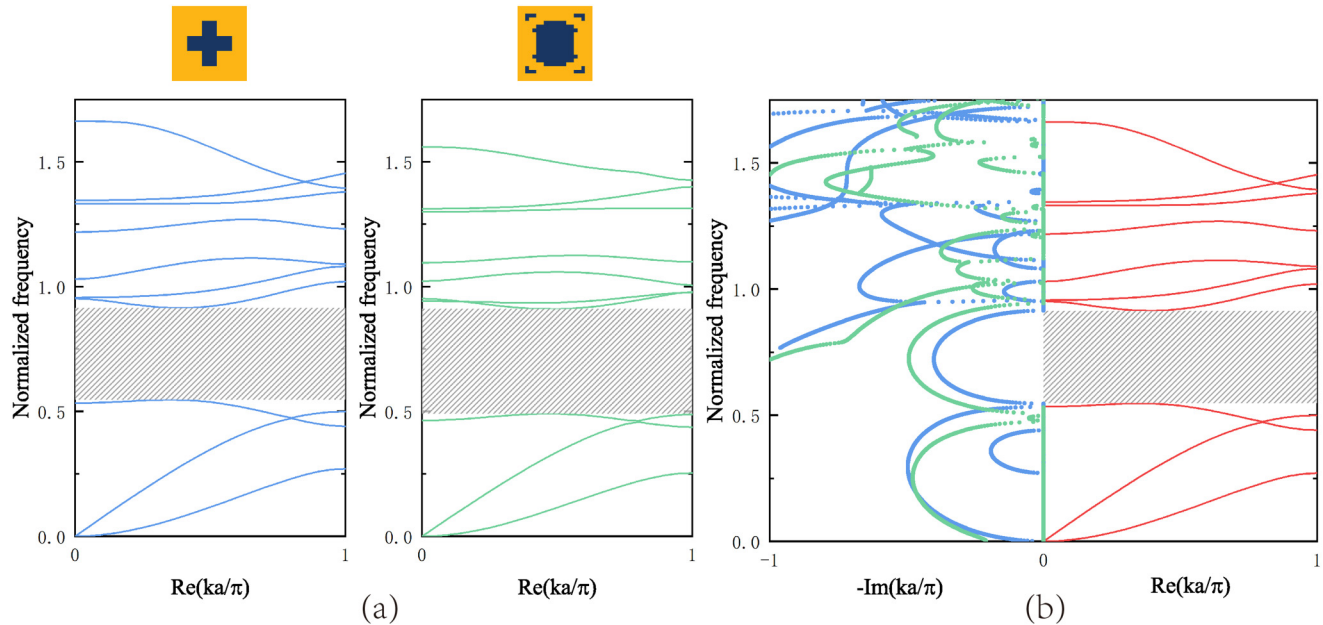
FIG. 6. Examples of the inverse design and comparison. (a) The two candidate topologies with similar first bandgaps. (b) The complex band structures of the two different topologies.

Fig. 1, a topological structure is inversely generated in the DL model, revealing the one-to-many nature of the design problem. At this point, one of the two suitable candidates can be selected to meet the additional requirement of greater spatial attenuation of evanescent waves. It is also an idea of optimization. The Per-SFE method is applied to figure the complex band structures of two different topologies by the $k(\omega)$ technique. The imaginary parts of wave numbers are drawn together for comparison, as shown in Fig. 6(b). Although the two topologies have similar first bandgaps, the imaginary part of wave numbers corresponding to the bandgap are different in size, and the positions where the maximum values appear are also different. In comparison, the evanescent waves experience greater spatial attenuation in the generated structure. Therefore, considering the application of acoustic insulation and vibration isolation, the generated structure should be preferred. It is vital to notice that due to the limitation of design space in this study, it is almost impossible to obtain two or more topologies with exactly the same band structure. More satisfactory results can be achieved by increasing the design space.

V. CONCLUSION

In this paper, a data-driven DL framework is applied to predict the band structure and inverse topological design of one-dimensional periodic two-dimensional tetragonal solid–solid PnCs with anticipated attenuation characteristics of elastic waves. Furthermore, a topological structure of a unit cell with larger spatial decay of evanescent waves under a similar first bandgap is selected by the $k(\omega)$ technique utilizing the Per-SFE approach. The trained CNN bypassed the numerical simulation process and predicted the band structures of PnCs directly and accurately by establishing a nonlinear mapping relationship between the topological structure features and the dispersion properties of PnCs. In addition, a topology with the closest approximation to the expected bandgap can be generated inversely by the neural network system. Afterward, the Per-SFE approach is utilized to compare the minimum imaginary part of wave numbers between different topological structures with similar first bandgap, screening the topology with the larger spatial attenuation performance of evanescent waves. Finally, an anticipated bandgap PnC topology is obtained, which has promising potential in the application of acoustic insulation and vibration isolation. However, this study is a preliminary exploration. This is still not perfect enough in the construction of datasets. The core of DL is the validity of constructing datasets. The topological structures of the unit cell are randomly generated by using the method of twice mirror symmetry with discrete grids of 20×20, which is insufficient to unlock the potential of DL. In future work, more complete topology generation rules and higher dimensional topology are demanded, which facilitates the inverse design and further expansion in one-to-many cases.

AUTHOR DECLARATIONS

Conflict of Interest

The authors have no conflicts to disclose.

Author Contributions

Sihao Han: Data curation (equal); Investigation (equal); Validation (equal); Visualization (equal); Writing – original draft (equal). **Qiang Han:** Conceptualization (equal); Funding acquisition (equal); Project administration (equal); Supervision (equal); Writing – review & editing (equal). **Chunlei Li:** Conceptualization (equal); Funding acquisition (equal); Methodology (equal); Supervision (equal); Writing – review & editing (equal).

DATA AVAILABILITY

The data that support the findings of this study are available from the corresponding author upon reasonable request.

REFERENCES

[1]M. S. Kushwaha, P. Halevi, L. Dobrzynski, and B. Djafari-Rouhani, "Acoustic band structure of periodic elastic composites," Phys. Rev. Lett. **71**, 2022 (1993).

[2]Y. Z. Wang, F. M. Li, K. Kishimoto, Y. S. Wang, and W. H. Huang, "Band gaps of elastic waves in three-dimensional piezoelectric phononic crystals with initial stress," Eur. J. Mech. A **29**, 182 (2010).

[3]R. Feng and K. Liu, "Tuning the band-gap of phononic crystals with an initial stress," Physica B **407**, 2032 (2012).

[4]X. Zhang and Z. Liu, "Negative refraction of acoustic waves in two-dimensional phononic crystals," Appl. Phys. Lett. **85**, 341 (2004).

[5]F. Yang, Z. Tan, X. Han, and C. Cho, "A graded negative refraction-index phononic crystals plate lens for focusing A0 mode lamb wave and energy harvesting," Results Phys. **31**, 105006 (2021).

[6]B. Liang, B. Yuan, and J. Cheng, "Acoustic diode: Rectification of acoustic energy flux in one-dimensional systems," Phys. Rev. Lett. **103**, 104301 (2009).

[7]Y. Chen, B. Wu, Y. Su, and W. Chen, "Tunable two-way unidirectional acoustic diodes: Design and simulation," J. Appl. Mech. **86**, 031010 (2019).

[8]J. Lu, C. Qiu, S. Xu, Y. Ye, and Z. Liu, "Dirac cones in two-dimensional artificial crystals for classical waves," Phys. Rev. B **89**, 134302 (2014).

[9]Z. Tian, C. Shen, J. Li, E. Reit, H. Bachman, J. E. S. Socolar, S. A. Cummer, and T. J. Huang, "Dispersion tuning and route reconfiguration of acoustic waves in valley topological phononic crystals," Nat. Commun. **11**, 1 (2020).

[10]M. S. Kushwaha, P. Halevi, G. Martinez, L. Dobrzynski, and B. Djafari-Rouhani, "Theory of acoustic band structure of periodic elastic composites," Phys. Rev. B **89**, 2313 (1994).

[11]Z. Liu, X. Zhang, Y. Mao, Y. Y. Zhu, Z. Yang, C. T. Chan, and S. Ping, "Locally resonant sonic materials," Science **289**, 1734 (2000).

[12]N. Kaina, M. Fink, and G. Lerosey, "Composite media mixing Bragg and local resonances for highly attenuating and broad bandgaps," Sci. Rep. UK **3**, 1 (2013).

[13]A. K. Sharma, M. M. Joglekar, D. M. Joglekar, and A. Zeeshan, "Topology optimization of soft compressible phononic laminates for widening the mechanically tunable band gaps," Compos. Struct. **289**, 115389 (2022).

[14]Y. Chen, X. Huang, G. Sun, X. Yan, and G. Li, "Maximizing spatial decay of evanescent waves in phononic crystals by topology optimization," Comput. Struct. **182**, 430 (2017).

[15]Y. Jiang, F. Meng, Y. Chen, Y. Zheng, and X. Huang, "Vibration attenuation analysis of periodic underground barriers using complex band diagrams," Comput. Geotech. **128**, 103821 (2020).

[16]V. Romero-García, J. V. Sánchez-Pérez, S. Castineira-Ibanez, and L. M. Garcia-Raffi, "Evidences of evanescent Bloch waves in phononic crystals," Appl. Phys. Lett. **96**, 124102 (2010).

[17]V. Romero-García, L. M. Garcia-Raffi, and J. V. Sánchez-Pérez, "Evanescent waves and deaf bands in sonic crystals," AIP Adv. **1**, 041601 (2011).

[18]V. Romero-García, J. O. Vasseur, L. M. Garcia-Raffi, and A. C. Hladky-Hennion, "Theoretical and experimental evidence of level repulsion states and evanescent modes in sonic crystal stubbed waveguides," New J. Phys. **14**, 023049 (2012).

[19]V. Laude, Y. Achaoui, S. Benchabane, and A. Khelif, "Evanescent Bloch waves and the complex band structure of phononic crystals," Phys. Rev. B **80**, 092301 (2009).

[20]I. A. Veres and T. Berer, "Complexity of band structures: Semi-analytical finite element analysis of one-dimensional surface phononic crystals," Phys. Rev. B **86**, 104304 (2012).

[21]C. L. Li, T. J. Jiang, S. Liu, and Q. Han, "Dispersion and band gaps of elastic guided waves in the multi-scale periodic composite plates," Aerosp. Sci. Technol. **124**, 107513 (2022).

[22]Y. Chen, F. Meng, G. Li, and X. Huang, "Designing photonic materials with complete band gaps by topology optimization," Smart Mater Struct. **28**, 015025 (2018).

[23]H. W. Dong, X. X. Su, Y. S. Wang, and C. Zhang, "Topological optimization of two-dimensional phononic crystals based on the finite element method and genetic algorithm," Struct. Multidiscip. **50**, 593 (2014).

[24]H. W. Dong, X. X. Su, and Y. S. Wang, "Multi-objective optimization of two-dimensional porous phononic crystals," J. Phys. D **47**, 155301 (2014).

[25]S. Halkjær, O. Sigmund, and J. S. Jensen, "Inverse design of phononic crystals by topology optimization," Z. Krist-Cryst. Mater. **220**, 895 (2005).

[26]S. M. Sadat and R. Y. Wang, "A machine learning based approach for phononic crystal property discovery," J. Appl. Phys. **128**, 025106 (2020).

[27]C. T. Chen and G. X. Gu, "Generative deep neural networks for inverse materials design using backpropagation and active learning," Adv. Sci. **7**, 1902607 (2020).

[28]C. X. Liu and G. L. Yu, "Inverse design of locally resonant metabarrier by deep learning with a rule-based topology dataset," Comput. Method. Appl. Mech. **394**, 114925 (2022).

[29]Y. Jin, L. He, Z. Wen, B. Mortazavi, H. Guo, D. Torrent, B. Djafari-Rouhani, T. Rabczuk, X. Zhuang, and Y. Li, "Intelligent on-demand design of phononic metamaterials," Nanophotonics-Berlin **11**, 439 (2022).

[30]X. Li, S. Ning, Z. Liu, Z. Yan, and Z. Zhuang, "Designing phononic crystal with anticipated band gap through a deep learning based data-driven method," Comput. Method. Appl. Mech. **361**, 112737 (2020).

[31]W. Jiang, Y. Zhu, G. Yin, H. Lu, L. Xie, and M. Yin, "Dispersion relation prediction and structure inverse design of elastic metamaterials via deep learning," Mater. Today Phys. **22**, 100616 (2022).

[32]I. Goodfellow, J. Pouget-Abadie, M. Mirza, B. Xu, D. Warde-Farley, S. Ozair, A. Courville, and Y. Bengio, "Generative adversarial networks," Commun. ACM **63**, 139 (2020).

[33]P. Isola, J. Y. Zhu, T. Zhou, and A. Efros, "Image-to-image translation with conditional adversarial networks," in *IEEE Conference on Computer Vision & Pattern Recognition (CVPR)* (IEEE, 2017), pp. 1125–1134.

[34]S. Yadav and S. Shukla, "Analysis of k-fold cross-validation over hold-out validation on colossal datasets for quality classification," in *2016 IEEE 6th International Conference on Advanced Computing (IACC)* (IEEE, 2016), pp. 78–83.